CHALMERS
UNIVERSITY OF TECHNOLOGY

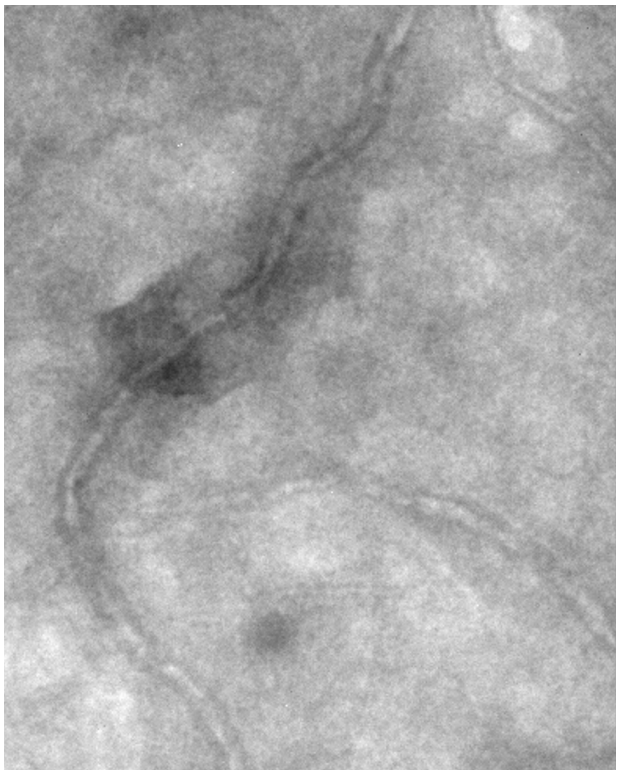

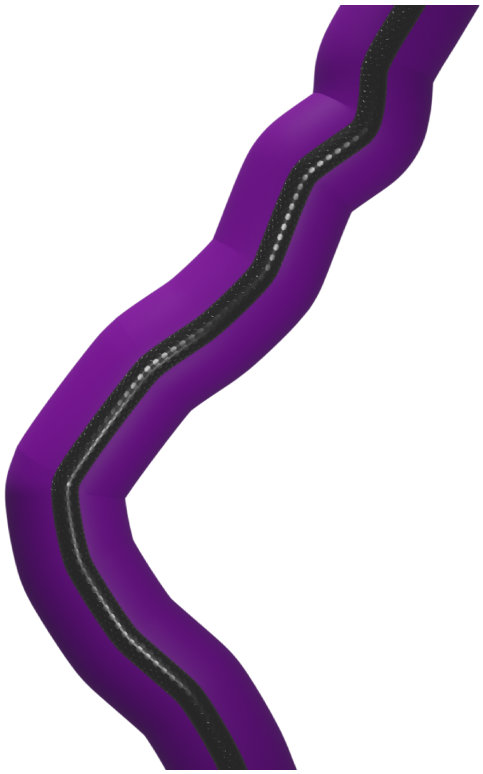

Microstructural study of a conducting polymer doped with carbon nanotubes

Master's thesis in Physics

Fredrik Söderberg

DEPARTMENT OF PHYSICS
CHALMERS UNIVERSITY OF TECHNOLOGY
Gothenburg, Sweden 2021
www.chalmers.se

Master's thesis 2021

Microstructural study of a conducting polymer doped with carbon nanotubes

Fredrik Söderberg

CHALMERS
UNIVERSITY OF TECHNOLOGY

Department of Physics
Nano and Biophysics
Eva Olsson Group
Chalmers University of Technology
Gothenburg, Sweden 2021

Microstructural study of a conducting polymer doped with carbon nanotubes

Supervisor: Eva Olsson, Department of Physics
Examiner: Eva Olsson, Department of Physics

Master's Thesis 2021
Department of Physics
Nano and Biophysics
Eva Olsson Group
Chalmers University of Technology
SE-412 96 Gothenburg
Telephone +46 31 772 1000

Typeset in LaTeX
Printed by Chalmers Reproservice
Gothenburg, Sweden 2021

Microstructural study of a conducting polymer doped with carbon nanotubes
Fredrik Söderberg
Department of physics
Chalmers University of Technology

Abstract

This work concerns the microsctructure of benzimidazobenzophenanthroline, BBL, films doped with carbon nanotubes, CNTs, to increase the electron mobility of the films. The CNT dopings were 1, 9 and 50 wt% respectively. The microsctructures were studied using electron microscopy including scanning electron microscopy and transmission electron microscopy. The morphology of the films gradually changed from a continuous BBL film with a relatively rough surface morphology in the 1 wt% films with randomly oriented CNTs to a structure with the BBL forming a smooth shell of BBL on the CNTs. The CNTs were multiwalled with a high density of defects. The thickness of the BBL shell was about 20-30 nm in the 1 and 9 wt% films and 3-4 nm in the 50 wt% films. The results show that the electron mobility can be even further increased by aligning the CNTs that have a considerably higher mobility along their long axis and also compared to the BBL. It should be noted that an alignment of the CNTs would also result in a high directional anisotropy of the mobility in the BBL:CNT films.

Keywords: BBL, CNT, SEM, STEM, TEM, SE, doped polymer films, microsctructure

Acknowledgements

I would like to thank my supervisor and examinator Eva Olsson for her suggestion of this research topic, her invaluable expertise in both theory and practice and the insightful discussions during this master's thesis.
I would also like to thank the Eva Olsson Group for the support and help during the thesis work. I would especially like to thank Gustav Persson, Rebecka Rilemark and Lunjie Zeng who have taken the time to discuss results, methods and introduced me to the instruments.
A thank you to Silan Zhang and Simone Fabiano who produced the samples. The experiments have all been performed at Chalmers Materials Analysis Labratory (CMAL) and I would like to thank the staff at CMAL for their helpfullness and answers.

Fredrik Söderberg, Gothenburg, August 2021

Contents

List of Figures

List of Tables

Abbreviations

SE	-	Secondary Electrons
BBL	-	benzimidazobenzophenanthroline
BF	-	Bright Field
BSE	-	Backscattered Electrons
CNT	-	Carbon Nanotubes
EDS	-	Energy-Dispersive X-ray Spectroscopy
HRTEM	-	High Resolution Transmission Electron Microscopy
IPA	-	Isopropyl Alcohol
LED	-	Lower Electron Detector
MSA	-	Methanesulfonic Acid
OECT	-	Organic Electrochemical Transistor
SEM	-	Scanning Electron Microscope
STEM	-	Scanning Transmission Electron Microscope
TED	-	Transmission Electron Detector
TEM	-	Transmission Electron Microscope
UED	-	Upper Electron Detector
wt	-	Weight

1

Introduction

Organic electronics can be tailored to match and interact with its surroundings [1], however, the conductivity of organic electronics is still much lower than that of traditional electronics. One type of organic electronic transistor is the organic electrochemical transistor, OECT. OECTs have been used to monitor extracellular electron transfer, neural interfaces, chemical and biological sensors and printable electronics [2–6]. In an OECT, an electrically conducting film, in contact with an electrolyte, creates the gate, see Fig. 1.1. Most researched OECTs are of p-type, however a complementary OECT, i.e. consisting of both n- and p-type, was recently published [7]. The n-type polymer used in the complementary OECT is benzimidazobenzophenanthroline, BBL. Sun et al. estimated the electron mobility in the BBL film in the complementary OECT to be $7 \times 10^{-4} \mathrm{cm}^2\mathrm{V}^{-1}\mathrm{s}^{-1}$, which still is low compared to traditional transistors [8]. Therefore, doping of the film to increase the electron mobility is of interest. The conducting polymer film studied in this thesis is BBL doped with carbon nanotubes. An increase of electron mobility has been observed, however due to the non-linear dependence of electron mobility with dopant concentration, it is important to correlate the dopant level to the microstructure and properties of the doped films.

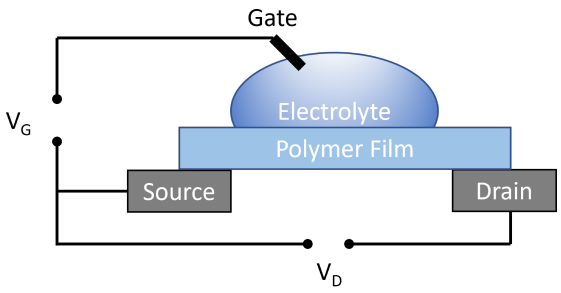

Figure 1.1: Schematic drawing of an organic electrochemical transistor

1.1 Microstructure and material properties

The microstructure of a material, is the description of the phases that are present, their morphology, size and spatial distribution. The microstructure directly effect materials properties on a wide spectrum of materials, from mechanical properties of steel such as hardness [9, 10] to the iridescence of butterfly wings [11, 12]. The microstructure is the underlying cause of the macroscopic properties. It is therefore

important to investigate the microstructure to understand the properties of the material.
The microstructure of a material can change with fabrication parameters, e.g. a thicker film may dry slower which means that a phase separation may progress for longer time before solidifying.

1.2 Limitations

This study concerns three BBL films with different CNT doping concentrations which are 1, 9 and 50 wt%. The films have been studied using electron microscopy. It offers high spatial resolution and site specific analysis. For site specific analysis it is important to determine what is representative for the films and avoid artifacts. Electron microscopy includes several imaging, diffraction and spectroscopy modes. This study uses scanning electron microscopy and transmission electron microscopy.

1.3 Aim and Goal

The aim of this project is to study the microstructure of BBL films doped with carbon nanotubes and characterize the effect of doping on the microstructure.

1.4 Ethical aspects

The wide range of applications of conductive polymers is due to the malleability of organic materials. E.g. OECT devices is tuned to be biocompability, leading the way to new diagnostics in health care and techniques in biological research. The drive for cheaper electronics promotes, the interest in conductive polymers and the possibility to use cheap manufacturing techniques to create printable electronics. Further research into longevity and toxicology of each film constituent is important, but not something that is taken into account in this study.

2
Materials and Methods

The samples examined in this study consist of three films of BBL doped with varying ratios of CNTs. The three ratios are: 1, 9 and 50 wt% CNT. The films are made at Linköping University where our collaboration partners are Simone Fabiano (Associate Professor, project leader) and Silan Zhang (PhD student).

2.1 Polymer films

BBL has a reported electron mobility of 0.1 $cm^2/(V\ s)$ [13]. BBL crystallizes into polycrystals consisting of stacked polymer sheets, Fig. 2.1, with a stacking repeating at 7.9 Å and sheet spacing of 3.7 Å [14–16].
PEDOT:PSS is a conducting polymer. The diffraction pattern of polycrystalline PEDOT:PSS shows diffraction peaks corresponding to a real spacing of 1.3 Å and 2.6 Å [17]. In contrast to BBL, PEDOT:PSS contains sulphur.

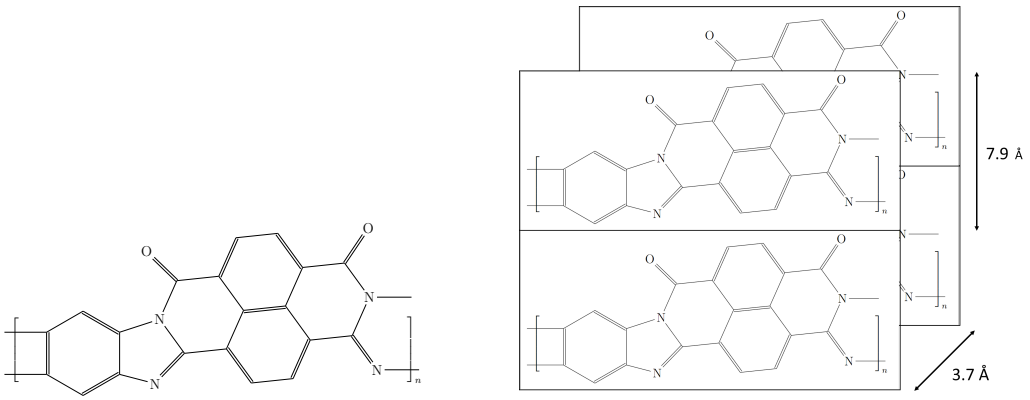

(a) Monomer of BBL **(b)** Crystal structure of BBL

Figure 2.1: Monomer and crystal structure for benzimidazobenzophenanthroline (BBL).

2.2 Carbon Nanotubes

Carbon nanotubes, CNTs, can be thought to be consisting of a sheet of graphene that is rolled up with connected ends of the sheet. CNTs can be divided into single-wall carbon nanotubes (SWCNT) and multi-walled carbon nanotubes (MWCNT) Fig. 2.2 [18]. The MWCNT consists of several SWCNTs inside one another.

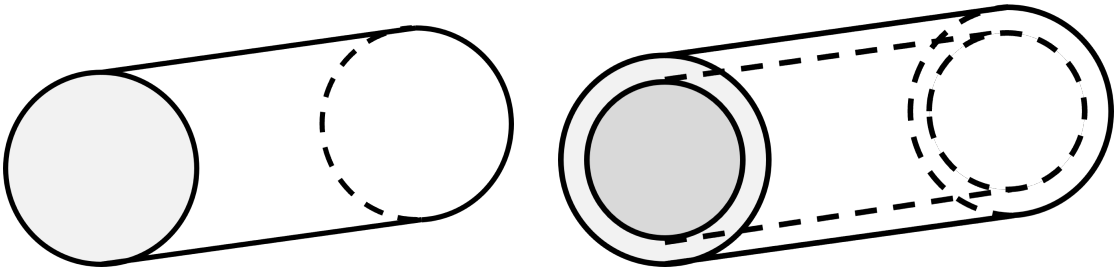

(a) Single-walled carbon nanotube **(b)** Multi-walled carbon nanotube

Figure 2.2: Schematic drawings of two types of carbon nanotubes.

The carbon-carbon spacing within the sheet in SWCNT is assumed to be the same as for graphite, 1.421 Å, or adjusted slightly due to the CNT curvature to 1.44 Å [18, 19]. For MWCNT the spacing between two carbon tubes is between 3.4 Å to 3.9 Å [18, 20–22]. Carbon nanotubes have shown to have a very high intrinsic mobility on the order of 100 000 $cm^2V^{-}1\ s^{-}1$ [23]. The mobility in CNTs is higher in the direction of the longitudinal axis, leading to anisotropic mobility of ordered CNTs [24].

2.3 BBL doped with carbon nanotubes

When BBL is doped with carbon nanotubes, the electron mobility increases as the doping ratio is increased, see Fig. 2.3. The increase in electron mobility is not linear with respect to CNT concentration, and far from the electron mobility of pure CNTs, which is 7 orders of magnitude higher, Fig. 2.3. The non-linearity is an indication that the microstructure of the material is important for the material properties. BBL has been reported to adhere to the MWCNTs as a shell [25].

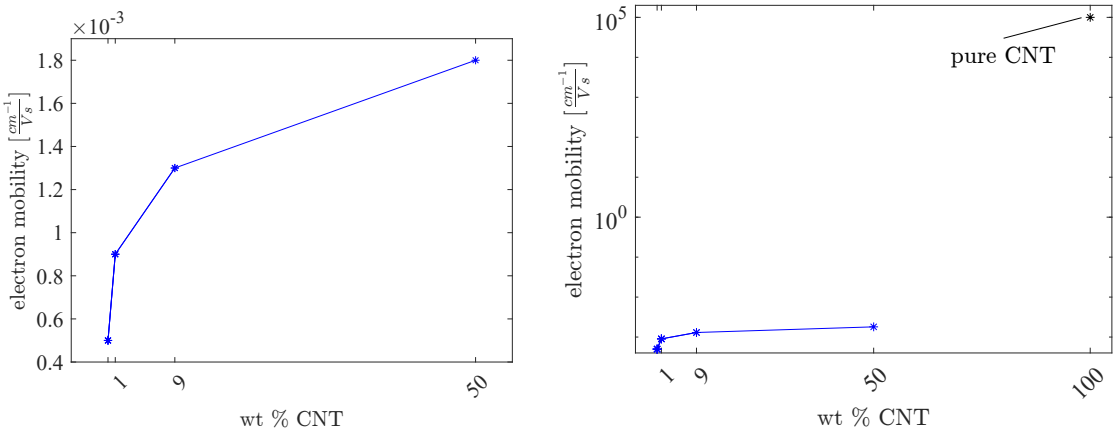

Figure 2.3: Electron mobility plotted against doping concentration
a) Electron mobility of pure BBL and BBL doped with CNTs
b) Electron mobility with pure CNTs included. Note the semi-log scale.

2.4 Sample preparation

The samples were prepared by Silan Zhang and Simone Fabiano at Linköping University. For large-scale BBL:CNT inks preparation, CNT was treated with acid and dispersed into isopropyl alcohol (IPA) solution. Then the BBL/MSA solution was poured into a CNT/IPA dispersion with rapid stirring. The BBL:CNT inks could be obtained after washing with water several times and redispersed in IPA. The BBL:CNT composite films were fabricated by simply spray-coating and annealing to remove residue solvent.
Each film is deposited on glass plates coated with the polymer PEDOT:PSS followed by the spray-coated BBL:CNT film. A scalpel is used to define smaller rectangles around a few mm^2, see Fig. 2.4. The glass plate is inserted in to deionized water which allows the films to float up to the surface. The films are lifted out of the water with a TEM 200 copper grid and left to air dry for a few minutes, Fig. 2.4.

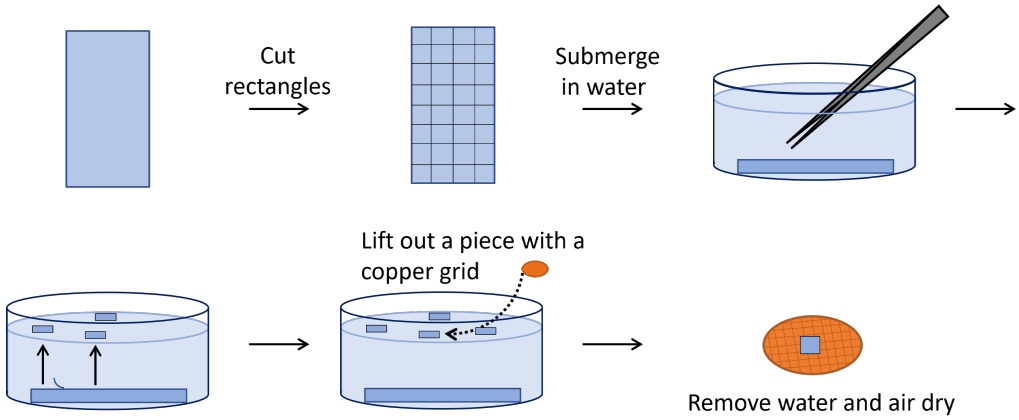

Figure 2.4: Sample preperation steps.

2.5 Electron Microscopy

In traditional optical microscopes, the resolution limit is approximated by the Rayleigh criterion. The Rayleigh criterion tells us that the resolution directly correlates to the wavelength of the light which we are probing with. Much like optical microscopes using photons to examine a sample, electron microscopes use electrons. Electrons are charged particles and interact with matter in a more complex way than photons. The wavelength of an electron is given by the de Broglie wave equation, Eq. 2.1

$$\lambda = \frac{h}{p} \tag{2.1}$$

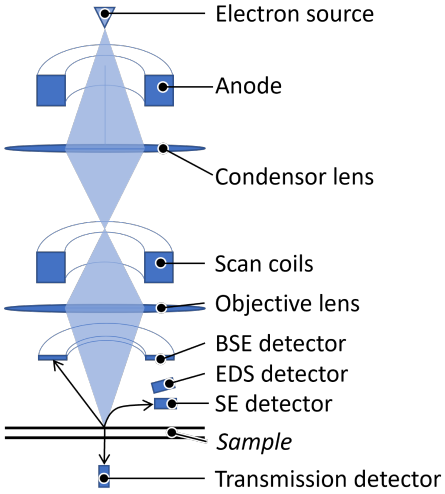

Figure 2.5: SEM Schematic drawing

where h is Planck's constant and p the particle momentum. The electrons used in electron microscopy have a wavelength that is much smaller than that of light in the visible spectra. The electron wavelength is decreased by its increasing momentum. The electron is a charged particle and can be accelerated by a potential (namely acceleration voltage) in the anode, thus decreasing the wavelength of the electron. The wavelength of an electron accelerated by the acceleration voltage is given by Eq. 2.2

$$\lambda = \frac{h}{\sqrt{2m_0 eV\left(1 + \frac{eV}{2m_0c^2}\right)}} \tag{2.2}$$

where m_0 is the rest mass of the electron, e is the electron charge, V the acceleration voltage and c the speed of light. A typical acceleration voltage for a transmission electron microscope is 200 kV, resulting a wavelength of 0.0025 nm, well below e.g. green light at around 550 nm. Practically, the resolution of electron microscopes is not close to the resolution limit due to lens aberrations, such as spherical aberration, and variation in wavelength from the electron source, i.e. the chromatic aberration. However, sub Ångström resolution is possible with modern microscopes, aberration corrections and experienced microscopists.
As the electron is a charged particle, it interacts with both the electron of the atoms and the nucleus.

2.6 Scanning electron microscopy

The theory on scanning electron microscopy provided here is based on the book "Scanning Electron Microscopy and X-ray Analysis" by Goldstein et al [26]. The scanning electron microscope, SEM, use an electron beam focused onto the sample, Fig. 2.6. Scan coils raster the beam over the sample while detectors extract the signals from the electrons interacting with the sample and a rastered image is obtained. When an electron hits a surface, several signals can be detected from the interaction between material and electron. The interaction volume, Fig. 2.7, is the volume in which the majority of the electron-matter interaction signals that reach the detector is generated. The size of the interaction volume determines the resolution of the recorded data. The interaction volume becomes larger with a higher acceleration voltage as higher energy electrons can penetrate deeper into the sample. Secondary

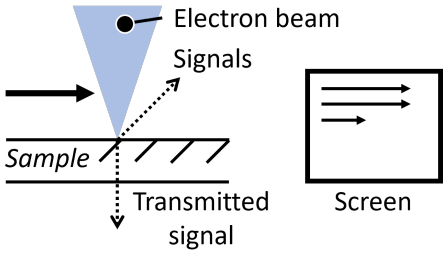

Figure 2.6: Schematic figure illustrating that a focused electron beam is rastered across the specimen in the SEM

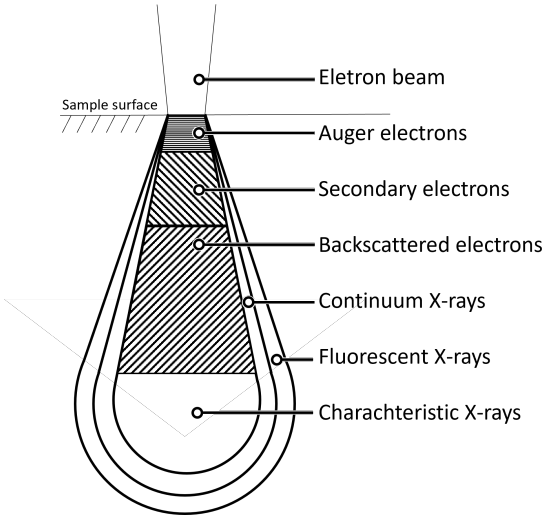

Figure 2.7: Interaction volume created by the electron beam hitting the sample surface. The different areas mark where a majority of the signals that reach the detector are produced.

electrons (SE) are electrons that escape from the atoms that are ionized by the electron beam, Fig. 2.8b. SE have significantly lower energy than the incident beam and they only escape the sample bulk if they are produced close to the surface. The SE signal is surface sensitive and tend to give back high resolution images.
Back scattered electrons (BSE) are primary electrons which are scattered at an angle of more than 90° with respect to the incident beam (this may include multiple scattering events), Fig. 2.8a. BSE are high energy electrons with energy close to the energy of the incident electrons. The BSE yield is higher for higher atomic num-

ber. BSE are therefore more sensitive to chemical composition as atoms with higher atomic number will become brighter in the BSE image. X-rays and Auger Electrons

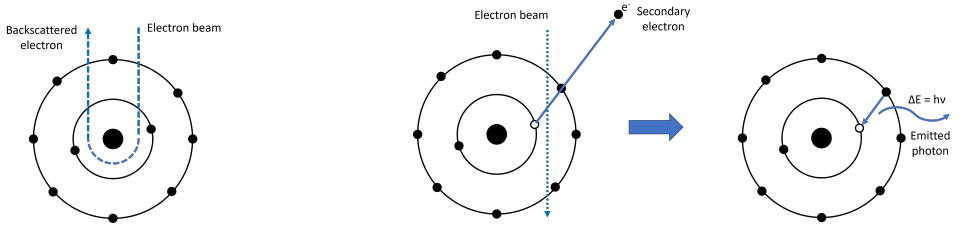

(a) Generation of backscattered electrons

(b) Generation of secondary electrons and characteristic X-ray

Figure 2.8: Generation of SE, BSE and characteristic X-rays

are generated after an inner shell electron has been ejected, Fig. 2.8b. An outer shell electron relaxes to the inner shell and a photon is emitted with energy equal to the energy difference between the two electron states. For X-rays, the energy of the photon is characteristic of the atom in which it was produced and so collecting these photons gives information about the chemical composition of the sample. The spatial resolution is of the order of a µm for a bulk specimen. The wavelength of the photons usually lie in the UV-spectra. These X-rays are called characteristic X-rays.
The emitted photon can be absorbed and eject an outer shell electron. Such electrons are called auger electrons. The intensity of characteristic X-rays and Auger electrons are inversely proportional. The technique of chemical characterization using characteristic X-rays is called energy-dispersive X-ray spectroscopy (EDS).
Bremsstrahlung consists of photons emitted due to the deceleration of the electrons. They are a major contributor to the background radiation when collecting characteristic X-ray spectra.
The most commonly used signals in a SEM are back scattered electrons, secondary electrons and X-rays. The secondary electron detector is often placed to the side of the sample, and the back scattered electron detector is placed above the sample. To filter the two types of electrons, a bias is applied at the secondary electron detector. The secondary electrons have lower energy than the back scattered electrons and the secondary electrons are attracted into the secondary electron detector by an applied bias at the detector. The high energy backscattered electrons have straight trajectories and continue up towards the back scattered electron detector, Fig. 2.5. If the sample thickness is small enough to allow transmission of electrons, the transmitted electron signal can be captured with a detector placed below the sample. This is called scanning transmission electron microscopy, STEM.
The SEM used in this study is a JEOL JSM-7800F Prime. The acceleration voltage used this study is 1 kV to 30 kV. The JEOL JSM-7800F Prime used is also equipped with a upper in column electron detector (UED) which use both BSE and SE to form an image, a lower electron detector (LED) which mainly use SE to form an image, a transmission electron detector (TED) which form an image from transmitted electrons and an energy dispersive X-ray (EDX) detector for capturing character-

istic X-rays. Investigation of the sample surface topography is performed using an acceleration voltage of 1 kV. The transmitted electron images and EDS spectra are obtain with an acceleration voltage of 30 kV.

2.7 Transmission Electron Microscopy

This chapter on transmission electron microscopy, TEM, is based on the book "Transmission Electron Microscopy" by Williams and Carter [27]. Electrons are transmitted through a thin sample. The electron beam in TEM consists of a parallel beam of electrons that are illuminating an area of the sample, rather than being rastered, Fig. 2.9. The electron-matter interaction for TEM is best understood by describing the electron as a wave. The electron beam is a wave that scatters in the sample. The image formed is a result of electrons diffracting and modulating the amplitude of the wave, or the phase. Mass thickness and diffraction contrast are examples of amplitude contrast. For mass-thickness contrast, electrons are more likely to scatter on atoms with higher atomic number, and a thicker sample will result in more scattering events. Phase contrast always includes two or more waves. One example of phase contrast is the interference between the electron wave scattered on the crystal lattice and the incident beam. This provides information about the atom planes in the structure.

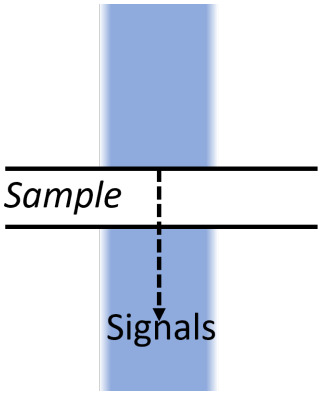

Figure 2.9: Schematic figure illustrating that a parallel electron beam is incident on the specimen in the TEM.

The diffraction from atom planes can be described by the Bragg equation, Eq. 2.3, where λ is the wavelength, n number of waves, d the atomic spacing and θ the angle of incident. From Braggs equation we see the important correlation between the scattering angle θ and the atomic plane distance d and arrangement, see Fig. 2.10.

$$n\lambda = 2dsin(\theta) \tag{2.3}$$

In imaging mode, Fig. 2.11a, the transmitted electrons are focused by magnetic lenses so that the image plane coincides with the detector plane.
Similarly, in diffraction mode the back focal plane coincides with the detector plane. Parallel rays from the specimen are focused onto the same spot in the back focal plane. Electrons scattered in identical angles, Bragg angles, creates a pattern specific to the crystal structure in the focal plane. The distance from the direct beam to a diffraction spot is $|G_{hkl}|$, which is inversely proportional to d_{hkl}, the distance to the plane (h,k,l), Eq. 2.4.

$$|G_{hkl}| = \frac{1}{|d_{hkl}|} \tag{2.4}$$

If two crystals are present, but rotated by an angle α, the resulting diffraction pattern show spots from both crystals, with an angle α between the patterns. For

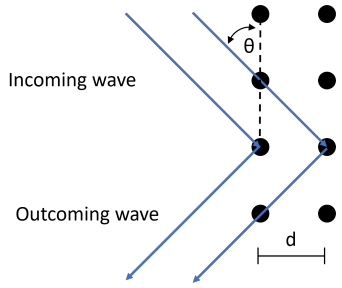

Figure 2.10: Schematic drawing of Bragg diffraction. Incoming electron wave scatters on a crystal lattice. The outgoing wave produce constructive interference if the Bragg condition is fulfilled.

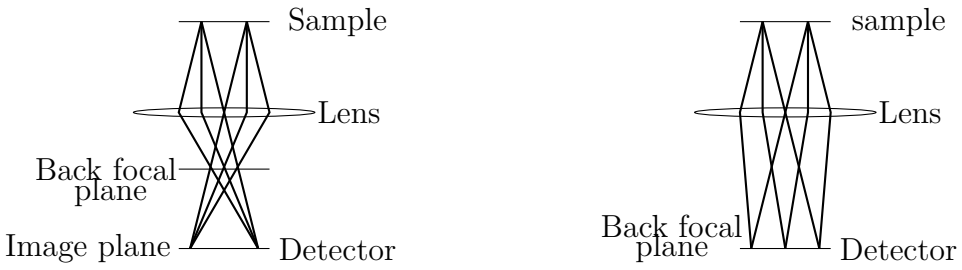

(a) Beam path for image formation. **(b)** Beam path for diffraction pattern.

Figure 2.11: The scattered electron beam can be focused onto the detector with an electromagnetic lens. By varying the strength of the electromagnetic lens it is possible to focus the image plane, (a), or the back focal plane (b).

polycrystalline materials the resulting pattern becomes ring formed, Fig. 2.13. An objective aperture is inserted in the back focal plane to filter out electrons scattered at higher angles. For bright field TEM (BFTEM), only the direct beam is selected. For high resolution TEM (HRTEM), the size of the aperture is selected to include one or more diffracted beams, see Fig. 2.12.
A gold pattern is used for calibration of the camera length. The inverse length per pixel can be calculated from the diffraction pattern of the gold pattern and then used to calculate the plane distance for the sample diffraction image. The reference diffraction pattern is taken during each session where diffraction patterns were obtained.
The TEM used in this study is a FEI Tecnai T20 with a LaB_6 filament in the electron gun. The FEI Tecnai T20 is also equipped with an EDAX-detector for capturing characteristic X-rays. The acceleration voltage is 200 kV.

(a) Aperture selection for BF **(b)** Aperture selection for HRTEM

Figure 2.12: Aperture selection in the back focal plane. The electron beams outside the aperture are blocked.

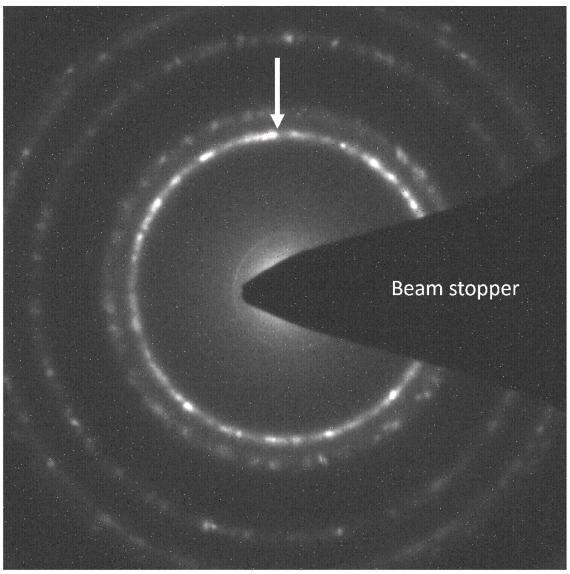

Figure 2.13: The electron diffraction pattern of gold, recorded at the TEM. The innermost ring (arrow) is due to diffraction spots from the $(1, 1, 1)$ plane from polycrystalline gold. The dark triangular feature is the beam stopper, inserted to protect the camera from the direct beam.

3
Results and Discussion

Three features can be distinguished in the films, namely the CNTs, the BBL and the support PEDOT:PSS film, see Fig. 3.1. BBL is distinguished by a rough surface, almost sponge like in appearance.

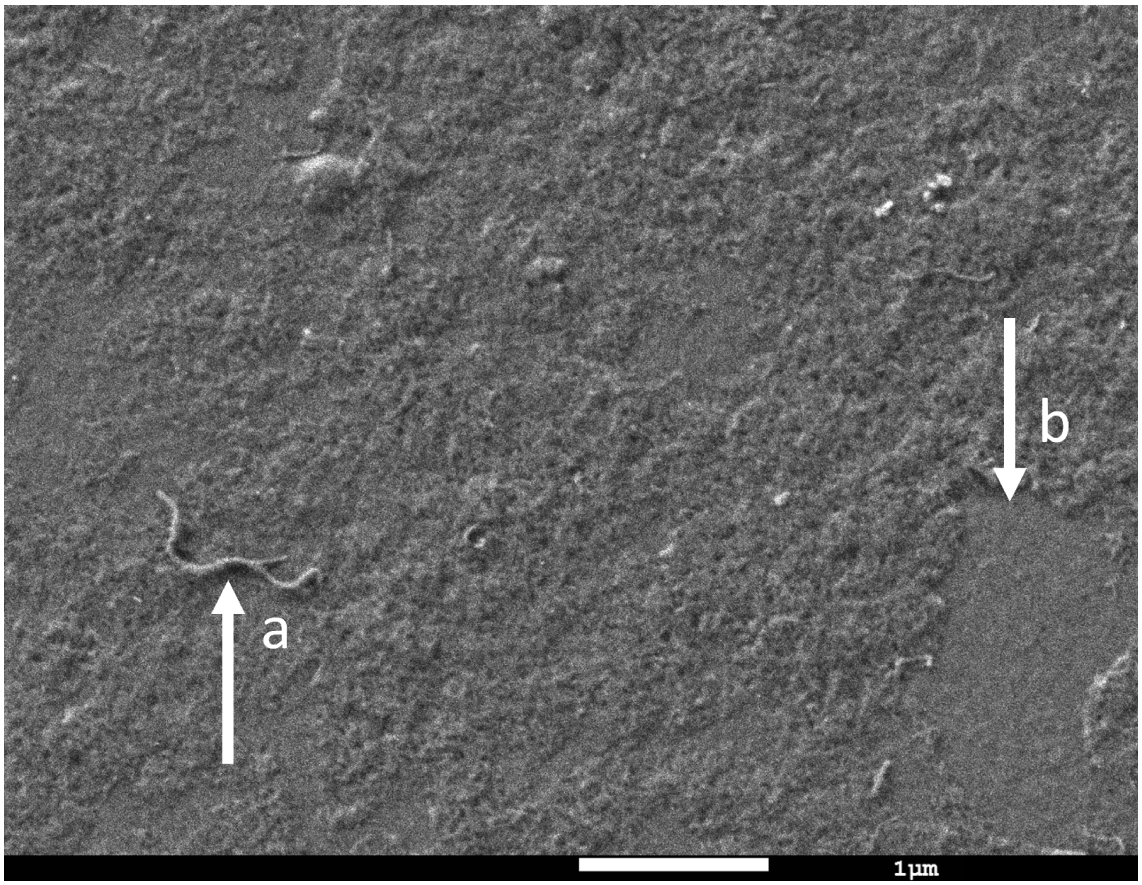

Figure 3.1: SEM image recorded with SE. A CNT is seen an elongated feature at a). The BBL polymer is covering the support film except for a few places. The underlying PEDOT:PSS support film is seen at b)

Comparing the morphology of the three films, we can see CNTs that are embedded in the BBL film in all samples, see Figs. 3.2 and 3.3. The support PEDOT:PSS film is more visible in the sample with 50 wt% CNT in areas with fewer CNTs, see Fig. 3.2. For the 50 wt% CNT only a few areas of BBL with the characteristic roughness can be identified, Fig. 3.3c.

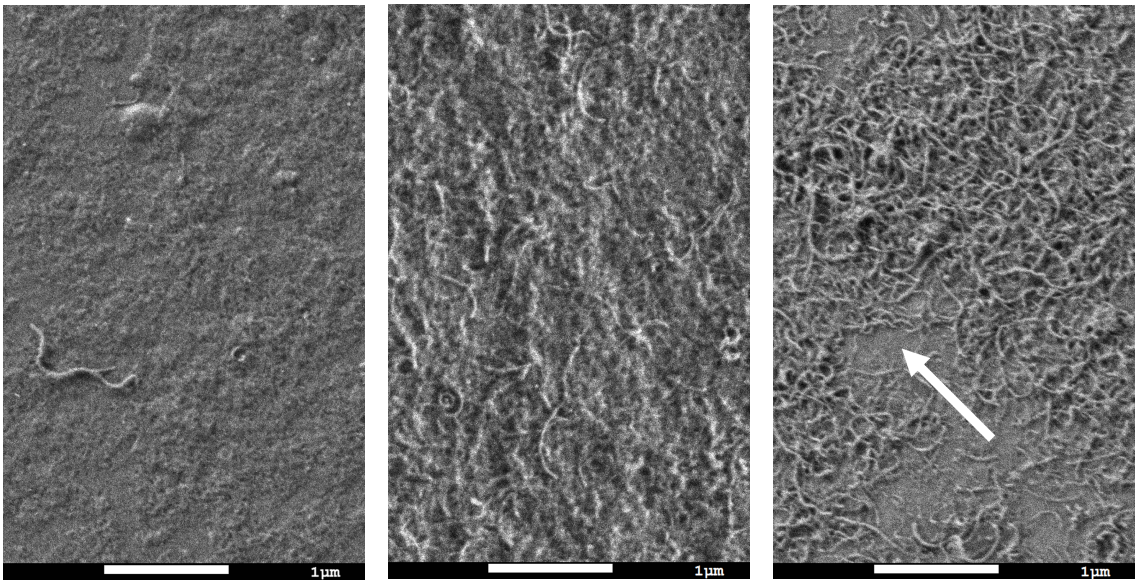

(a) 1 wt% CNT **(b)** 9 wt% CNT **(c)** 50 wt% CNT

Figure 3.2: SEM images recorded with with SE. Images show the morphology of the three films.
a) 1 wt% CNT The morphology of BBL is visible.
b) 9 wt% CNT The CNTs are covered in BBL.
c) 50 wt% CNT Almost no BBL film can be seen. The underyling PEDOT:PSS film is visible where there are fewer CNTs (arrow).

Further information about the microstructure of the films is revealed by TEM. Fig. 3.4 shows a CNT in BFTEM. Fig. 3.5b shows a typical morphology of the 9 wt% CNT film imaged using BFTEM. The CNTs are seen as elongated features in the image. The surrounding areas have a varying intensity. The intensity level is lower adjacent to the nanotubes while there is a higher intensity level further away. This can be compared to the SEM data where the CNTs are associated with a more rough surface morphology and there are patches with bare PEDOT:PSS. The higher intensity background in Fig. 3.5 corresponds therefore to PEDOT:PSS and the lower intensity areas are BBL. This is also supported by EDS analysis that show a lower sulphur to oxygen ratio in the low intensity areas compared to the high intensity areas.

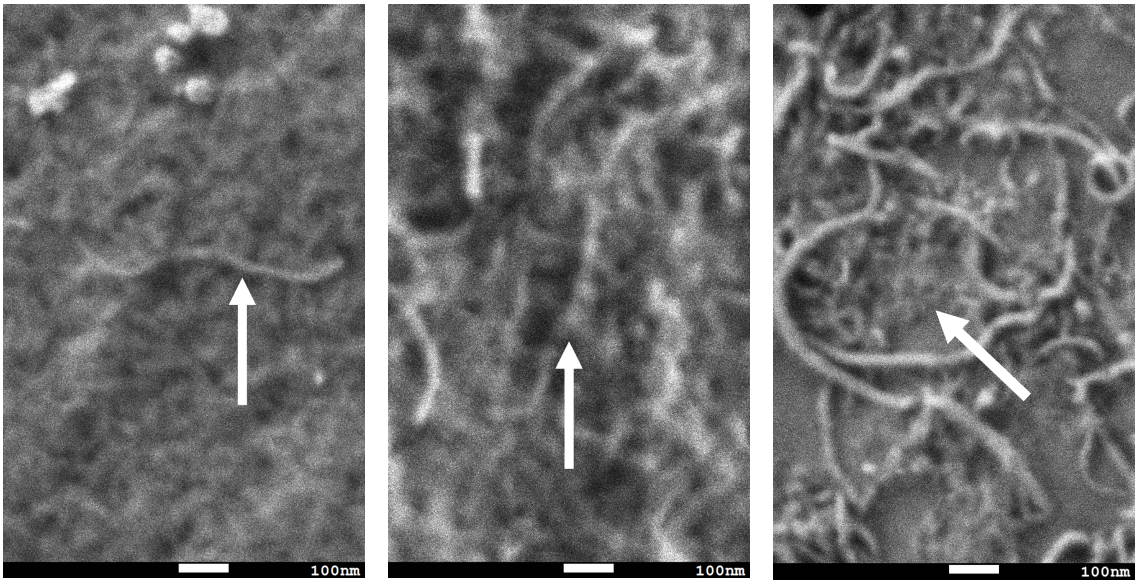

(a) 1 wt% CNT **(b)** 9 wt% CNT **(c)** 50 wt% CNT

Figure 3.3: SEM images recorded with SE.
a) A single CNT is seen in the BBL film (arrow).
b) The CNTs are going in and out of the BBL film (arrow).
c) A small patch of BBL is visible (arrow) between the CNTs.

The change in the microstructure of the films with increasing CNTs doping level is shown in Fig. 3.6. In the 1 wt% CNT there are rather large areas with the darker intensity level which also have a more uniform intensity level. The intensity level in the BBL varies more in 9 wt% CNT and in 50 wt% CNT the BBL is more predominantly located in the close vicinity of the CNTs.
A closer inspection of the CNTs also shows that there is a shell of BBL surrounding the CNTs, see Fig. 3.6. The shell thickness varies with CNT doping level and is smallest in the 50 wt% CNT where it is about 3-4 nm while it is about 20-30 nm in 9 wt% CNT, see Fig. 3.7. There are fewer measurement points in 1 wt% CNT but the thickness is of the same order as for 9 wt% CNT, see Table 3.1. The BBL shell surface is less rough than the film BBL surface, see Fig. 3.3. The CNTs are multiwalled with wall thickness of about 2-5 nm corresponding to 5 to 15 walls, and a intershell spacing of about 3.8 Å see Fig. 3.8. High resolution TEM showed a high density of defects along the CNTs, see 3.8. The CNTs are randomly distributed in the film. Based on the fact that the mobility is higher along the axis of CNTs compared to the radial direction, this implies that the electron mobility can be further increased by aligning the CNTs. However, this would also give rise to a directional anisotropy of the mobility of the BBL:CNT films.

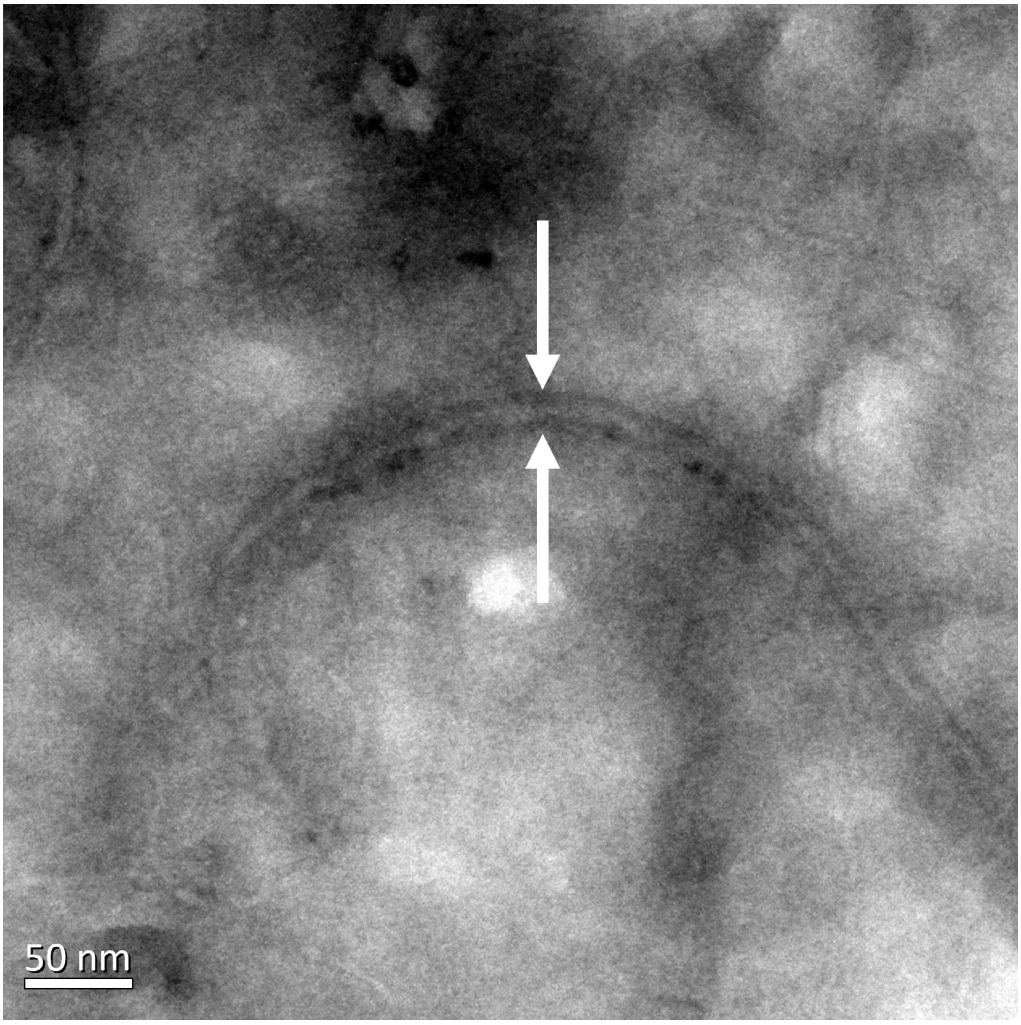

Figure 3.4: TEM BF image
The CNTs are seen as two lines with lower intensity contrast running along the CNT, marked by arrows. The center of the CNT has a higher intensity.

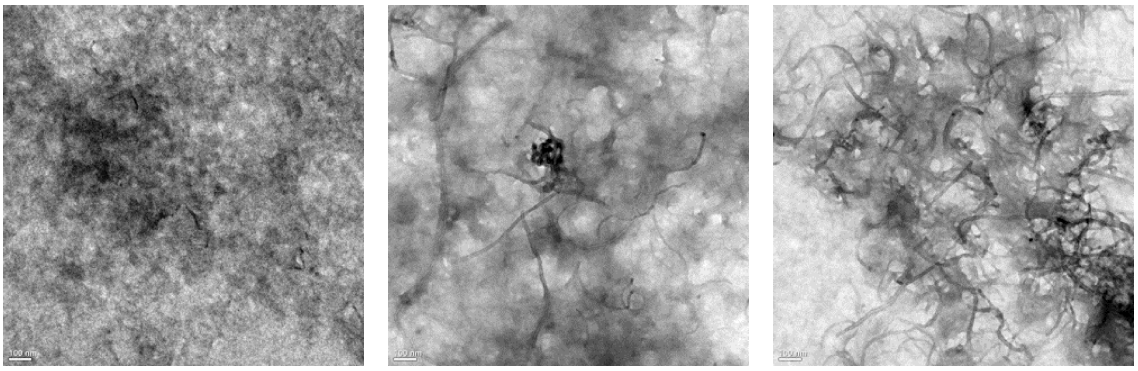

(a) 1 wt% CNT **(b)** 9 wt% CNT **(c)** 50 wt% CNT

Figure 3.5: TEM BF comparison images of the three films. CNTs can be seen as elongated features.
a) The dark contrast is due to BBL. BBL have a relatively uniform distribution.
b) The intensity level shows a higher variation than for 1 wt%.
c) The BBL is predominantly located in close vicinity of the CNTs. The areas with a high intensity are the PEDOT:PSS support film.

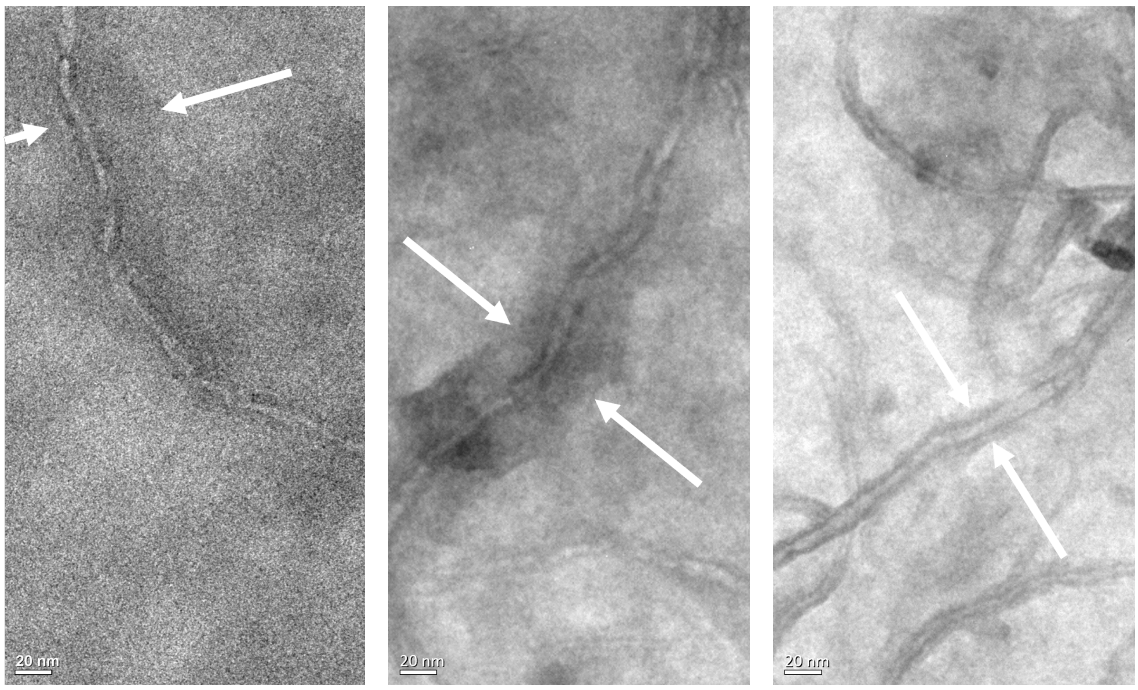

(a) 1 wt% CNT **(b)** 9 wt% CNT **(c)** 50 wt% CNT

Figure 3.6: TEM BF showing BBL layers around CNT. The dark contour around the CNTs, marked by arrows, is the BBL layer around the CNTs. The BBL layer is thinner for sample 50 wt%.

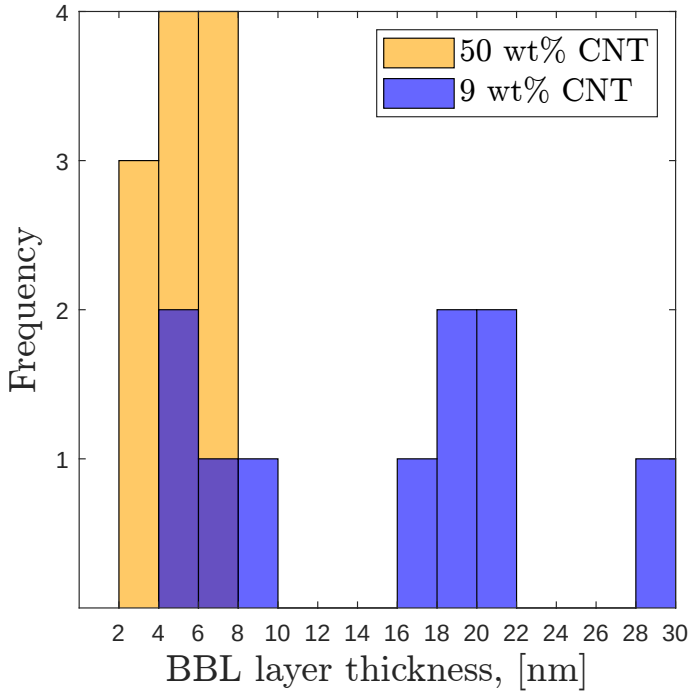

Figure 3.7: BBL shell thickness distribution for 9 and 50 wt%.

1 wt% CNT		9 wt% CNT		50 wt% CNT	
CNT diameter (nm)	BBL layer thickness (nm)	CNT diameter (nm)	BBL layer thickness (nm)	CNT diameter (nm)	BBL layer thickness (nm)
19.2	18.4	15.7	26	9.1	2.8
13.8	29.2	23	15.5	10	4.4
11.3	13.6	19[1]	26[1]	12.3	3.3
		9.6[1]	18[1]	11.6	6.0
		11.6	4.7	9.3	4.9
		13.5	20.9	10.1	2.6
		13.8	20.5	9.0	2.8
		11.4	18.1	9.1	5.6
		10.2	4.8	9.0	5.5
		11.3	8.0	8.0	6.5
		12.5	16.3	7.5	3.1
		11.3	8.6	7.8	4.4
		9.1	19.3	11.1	7.2
		8.8	28.6	8.3	6.6

Table 3.1: Table of measured CNT diameter and corresponding BBL shell layer thickness
[1]Measurement performed on STEM and SEM images. All other measurements are performed in TEM.

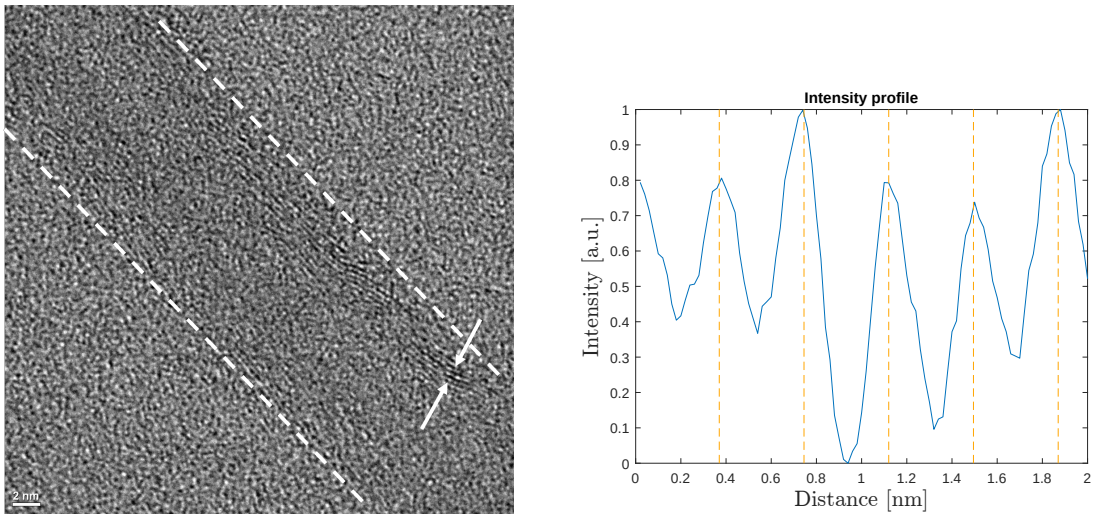

(a) **(b)**

Figure 3.8: a) HRTEM image of a CNT. The CNT is outlined (dashed line). The arrows mark lattice fringes from the CNT. The black and white background is due to BBL. The curvy lattice fringes and broken lines are indicative of defects.
b) The intensity profile is taken between the arrows. The profile is overlaid with the wall spacing of 0.375 nm.

4

Conclusion

The microstructure of benzimidazobenzophenanthroline, BBL, films doped with carbon nanotubes, CNTs, have been studied using electron microscopy in combination with energy dispersive x-ray spectroscopy (EDS). The electron microscopy was carried out using both scanning electron microscopy (SEM) and transmission electron microscopy (TEM). The purpose of doping the films with CNTs was to increase the electron mobility. The resulting mobility is determined by both the mobility of the individual constituents, i.e. BBL and CNT, as well as the distribution and morphology of the two constituents. The interfaces between the constituents can also significantly influence the transport properties. The SEM and TEM showed that the film structure gradually changed from a BBL film with pronounced surface roughness with occasional CNTs to a film that is dominated by CNTs covered by a relatively smooth BBL shell as the CNT doping changes from 1 wt% to 50 wt% CNT. The thickness of the BBL shell changes from 20-30 nm for the 1 wt% and 9 wt% CNT films to 3-4 nm for the 50 wt% CNT film. The CNTs are multiwalled with a high density of internal defects. The CNT/BBL core shell structures are randomly distributed in the films. The fact that the electron mobility is higher in the CNTs compared to the BBL and also that the mobility in the CNTs is higher along the long axis of the CNTs, implies that the mobility can be further increased by aligning the CNTs. This would, however, also give rise to a pronounced anisotropy of the BBL:CNT films.

5
Future work

During this thesis several ideas have been discussed and a few of these are listed here as suggestions for future work.
Performing a cross section of the BBL:CNT films to gain more information about the interface between BBL and CNTs.
Thin film BBL have been reported to form layered structures where the sheets are perpendicular to the surface [14]. The change in surface roughness between the smooth PEDOT:PSS and curved CNTs may be explained by studying the orientation of BBL around the CNTs.
More measurements of the BBL layer thickness around the CNTs and the shape of the thickness distribution of 9 wt% may give insight into the layer formation and structure around the CNTs.

Bibliography

(1) Berggren, M.; Richter-Dahlfors, A. *Advanced Materials* **2007**, *19*, 3201–3213.

(2) Méhes, G.; Roy, A.; Strakosas, X.; Berggren, M.; Stavrinidou, E.; Simon, D. T. *Advanced Science* **2020**, *7*, 1–8.

(3) Khodagholy, D.; Doublet, T.; Quilichini, P.; Gurfinkel, M.; Leleux, P.; Ghestem, A.; Ismailova, E.; Hervé, T.; Sanaur, S.; Bernard, C.; Malliaras, G. G. *Nature Communications* **2013**, *4*, DOI: 10.1038/ncomms2573.

(4) Lin, P.; Yan, F. *Advanced Materials* **2012**, *24*, 34–51.

(5) Nilsson, D.; Robinson, N.; Berggren, M.; Forchheimer, R. *Advanced Materials* **2005**, *17*, 353–358.

(6) Rivnay, J.; Inal, S.; Salleo, A.; Owens, R. M.; Berggren, M.; Malliaras, G. G. *Nature Reviews Materials* **2018**, *3*, DOI: 10.1038/natrevmats.2017.86.

(7) Sun, H.; Vagin, M.; Wang, S.; Crispin, X.; Forchheimer, R.; Berggren, M.; Fabiano, S. *Advanced Materials* **2018**, *30*, 1–7.

(8) Pengelly, R. S.; Wood, S. M.; Milligan, J. W.; Sheppard, S. T.; Pribble, W. L. *IEEE Transactions on Microwave Theory and Techniques* **2012**, *60*, 1764–1783.

(9) Zaefferer, S.; Ohlert, J.; Bleck, W. *Acta Materialia* **2004**, *52*, 2765–2778.

(10) Hossain, R.; Pahlevani, F.; Sahajwalla, V. *Scientific Reports* **2020**, *10*, 1–13.

(11) Vukusic, P.; Sambles, J. R.; Lawrence, C. R.; Wootton, R. J. *Proceedings of the Royal Society B: Biological Sciences* **1999**, *266*, 1403–1411.

(12) Ding, Y.; Xu, S.; Wang, Z. L. *Journal of Applied Physics* **2009**, *106*, DOI: 10.1063/1.3239513.

(13) Babel, A.; Jenekhe, S. A. *Journal of the American Chemical Society* **2003**, *125*, 13656–13657.

(14) Song, H. H.; Fratini, A. V.; Chabinyc, M.; Price, G. E.; Agrawal, A. K.; Wang, C. S.; Burkette, J.; Dudis, D. S.; Arnold, F. E. *Synthetic Metals* **1995**, *69*, 533–535.

(15) Babel, A.; Jenekhe, S. A. *Advanced Materials* **2002**, *14*, 371–374.

(16) Briseno, A. L.; Kim, F. S.; Babel, A.; Xia, Y.; Jenekhe, S. A. *Journal of Materials Chemistry* **2011**, *21*, 16461–16466.

(17) Zhou, J.; Anjum, D. H.; Chen, L.; Xu, X.; Ventura, I. A.; Jiang, L.; Lubineau, G. *Journal of Materials Chemistry C* **2014**, *2*, 9903–9910.

(18) Belin, T.; Epron, F. *Materials Science and Engineering B: Solid-State Materials for Advanced Technology* **2005**, *119*, 105–118.

(19) Wildoer, J. W. G.; Venema, L. C.; Rinzler, A. G.; Smalley, R. E.; Dekker, C. *Nature* **1998**, *391*, 59–61.

(20) Lijima, S. *Nature* **1991**, *354*, 56–58.

(21) Sun, X.; Kiang, C. H.; Endo, M.; Takeuchi, K.; Furuta, T. *Physical Review B - Condensed Matter and Materials Physics* **1996**, *54*, R12629–R12632.

(22) Bretz, M.; Demczyk, B. G.; Zhang, L. *Journal of Crystal Growth* **1994**, *141*, 304–309.

(23) Dürkop, T.; Getty, S. A.; Cobas, E.; Fuhrer, M. S. *Nano Letters* **2004**, *4*, 35–39.

(24) Hecht, D. S.; Hu, L.; Irvin, G. *Advanced Materials* **2011**, *23*, 1482–1513.

(25) Donaldson, E.; Durstock, M. F.; Taylor, B. E.; Tomlin, D. W.; Richardson, L. C.; Baur, J. W. *Organic Photovoltaics II* **2002**, *4465*, 85–93.

(26) Goldstein, J. I.; Newbury, D. E.; Michael, J. R.; Ritchie, N. W. M.; Scott, J. H. J.; Joy, D. C., *Scanning Electron Microscopy and X-Ray Microanalysis*, Fourth; Springer US: 2018.

(27) Williams, D. B.; Carter, C. B., *Transmission Electron Microscopy*, Second; Springer: 2009.

DEPARTMENT OF PHYSICS
CHALMERS UNIVERSITY OF TECHNOLOGY
Gothenburg, Sweden
www.chalmers.se

CHALMERS
UNIVERSITY OF TECHNOLOGY